5. Y. V. Shtogun, L. M. Woods, . *J. Phys. Chem. Lett.* **1**, 1356–1362 (2010).
6. W. Gao, A. Tkatchenko, *Phys. Rev. Lett.* **114**, 096101 (2015).
7. A. M. Reilly, A. Tkatchenko, *Phys. Rev. Lett.* **113**, 055701 (2014).
8. N. Ferri, R. A. DiStasio Jr., A. Ambrosetti, R. Car, A. Tkatchenko, *Phys. Rev. Lett.* **114**, 176802 (2015).
9. A. J. Stone, *The Theory of Intermolecular Forces* (Oxford Univ. Press, ed. 2, 2013).
10. E. M. Lifshitz, *Sov. Phys. JETP* **2**, 73 (1956).
11. S. Grimme, *WIREs Comput. Mol. Sci.* **1**, 211–228 (2011).
12. A. Tkatchenko, M. Scheffler, *Phys. Rev. Lett.* **102**, 073005 (2009).
13. C. A. Silvera Batista, R. G. Larson, N. A. Kotov, *Science* **350**, 1242477 (2015).
14. P. Loskill *et al.*, *Adv. Colloid Interface Sci.* **179–182**, 107–113 (2012).
15. P. Loskill *et al.*, *J. R. Soc. Interface* **10**, 20120587 (2013).
16. S. Tsoi *et al.*, *ACS Nano* **8**, 12410–12417 (2014).
17. G. A. Rance, D. H. Marsh, S. J. Bourne, T. J. Reade, A. N. Khlobystov, *ACS Nano* **4**, 4920–4928 (2010).
18. C. Wagner *et al.*, *Nat. Commun.* **5**, 5568 (2014).
19. D. B. Chang, R. L. Cooper, J. E. Drummond, A. C. Young, *Phys. Lett. A* **37**, 311–312 (1971).
20. M. Boström, B. E. Sernelius, *Phys. Rev. B* **61**, 2204–2210 (2000).
21. J. F. Dobson, A. White, A. Rubio, *Phys. Rev. Lett.* **96**, 073201 (2006).
22. J. F. Dobson, T. Gould, G. Vignale, *Phys. Rev. X* **4**, 021040 (2014).
23. A. J. Misquitta, J. Spencer, A. J. Stone, A. Alavi, *Phys. Rev. B* **82**, 075312 (2010).
24. A. J. Misquitta, R. Maezono, N. D. Drummond, A. J. Stone, R. J. Needs, *Phys. Rev. B* **89**, 045140 (2014).
25. A. Tkatchenko, R. A. DiStasio Jr., R. Car, M. Scheffler, *Phys. Rev. Lett.* **108**, 236402 (2012).
26. J. Applequist, K. R. Sundberg, M. L. Olson, L. C. Weiss, *J. Chem. Phys.* **70**, 1240 (1979).
27. W. L. Bade, *J. Chem. Phys.* **27**, 1280 (1957).
28. A. G. Donchev, *J. Chem. Phys.* **125**, 074713 (2006).
29. A. Ambrosetti, A. M. Reilly, R. A. DiStasio Jr., A. Tkatchenko, *J. Chem. Phys.* **140**, 18A508 (2014).
30. A. Tkatchenko, A. Ambrosetti, R. A. DiStasio Jr., *J. Chem. Phys.* **138**, 074106 (2013).
31. A. P. Jones, J. Crain, V. P. Sokhan, T. W. Whitfield, G. J. Martyna, *Phys. Rev. B* **87**, 144103 (2013).
32. A. M. Reilly, A. Tkatchenko, *J. Phys. Chem. Lett.* **4**, 1028–1033 (2013).
33. A. Ambrosetti, D. Alfè, R. A. DiStasio Jr., A. Tkatchenko, *J. Phys. Chem. Lett.* **5**, 849–855 (2014).
34. R. A. DiStasio Jr., O. A. von Lilienfeld, A. Tkatchenko, *Proc. Natl. Acad. Sci. U.S.A.* **109**, 14791–14795 (2012).
35. R. A. DiStasio Jr., V. V. Gobre, A. Tkatchenko, *J. Phys. Condens. Matter* **26**, 213202 (2014).
36. J. F. Dobson, J. Wang, B. P. Dinte, K. McLennan, H. M. Le, *Int. J. Quantum Chem.* **101**, 579–598 (2005).
37. V. V. Gobre, A. Tkatchenko, *Nat. Commun.* **4**, 2341 (2013).
38. R.-F. Liu, J. G. Ángyán, J. F. Dobson, *J. Chem. Phys.* **134**, 114106 (2011).
39. M. Dion, H. Rydberg, E. Schröder, D. C. Langreth, B. I. Lundqvist, *Phys. Rev. Lett.* **92**, 246401 (2004).
40. K. Berland *et al.*, *Rep. Prog. Phys.* **78**, 066501 (2015).
41. J. Dai, J. Yuan, P. Giannozzi, *Appl. Phys. Lett.* **95**, 232105 (2009).
42. P. A. Denis, *Chem. Phys. Lett.* **508**, 95–101 (2011).
43. J. Tao, J. P. Perdew, *J. Chem. Phys.* **141**, 141101 (2014).
44. L. J. Lis, M. McAlister, N. Fuller, R. P. Rand, V. A. Parsegian, *Biophys. J.* **37**, 667–672 (1982).
45. K. Autumn *et al.*, *Nature* **405**, 681–685 (2000).
46. See supplementary materials on *Science* Online.

ACKNOWLEDGMENTS

Supported by a startup grant from Cornell University (R.A.D.), European Research Council Starting Grant VDW-CMAT, and DFG/SFB-951 HIOS project A10. A.A. thanks F. Toigo and P. L. Silvestrelli for useful discussions. This research used resources of the Argonne Leadership Computing Facility at Argonne National Laboratory, which is supported by the Office of Science of the U.S. Department of Energy under contract DE-AC02-06CH11357.

SUPPLEMENTARY MATERIALS

www.sciencemag.org/content/351/6278/1171/suppl/DC1
Theoretical Methods
Supplementary Text
Tables S1 to S3

10 December 2015; accepted 31 January 2016
10.1126/science.aae0509

REPORTS

QUANTUM OPTICS

Generation of multiphoton entangled quantum states by means of integrated frequency combs

Christian Reimer,[1]* Michael Kues,[1]*† Piotr Roztocki,[1] Benjamin Wetzel,[1,2] Fabio Grazioso,[1] Brent E. Little,[3] Sai T. Chu,[4] Tudor Johnston,[1] Yaron Bromberg,[5]‡ Lucia Caspani,[6]§ David J. Moss,[7]|| Roberto Morandotti[1,8]†

Complex optical photon states with entanglement shared among several modes are critical to improving our fundamental understanding of quantum mechanics and have applications for quantum information processing, imaging, and microscopy. We demonstrate that optical integrated Kerr frequency combs can be used to generate several bi- and multiphoton entangled qubits, with direct applications for quantum communication and computation. Our method is compatible with contemporary fiber and quantum memory infrastructures and with chip-scale semiconductor technology, enabling compact, low-cost, and scalable implementations. The exploitation of integrated Kerr frequency combs, with their ability to generate multiple, customizable, and complex quantum states, can provide a scalable, practical, and compact platform for quantum technologies.

Multi-entangled states of light hold answers to fundamental questions in quantum physics and are the cornerstone of a range of applications, including quantum communications (*1*), computation (*2*–*4*), and sensing and imaging with a resolution beyond the classical limit (*5*). Thus, the controllable realization of multiple quantum states in a compact platform would enable a practical and powerful implementation of quantum technologies. Although applications of frequency combs have been mostly classical thus far, their distinctive architecture, based on multiple interacting modes and the phase characteristics of the underlying nonlinear processes, has the potential to offer new and powerful ways to achieve the generation of multiple, customizable, and complex states of nonclassical light. The quantum properties of frequency combs have recently begun to be investigated, revealing their potential for the generation of large quantum states (*6*–*8*). However, the continuous-variable nonclassical states (squeezed vacuum) that have been demonstrated with this approach have not yet achieved the quality (amount of squeezing) required for optical quantum computation (*9*). For the generation of single photons and continuous- and discrete-variable quantum states (qubits), a wide variety of second- and third-order nonlinear sources, optical fibers, and gases, as well as single quantum emitters, have been exploited (*10*, *11*). Recent progress has focused on transferring both classical frequency combs (*12*) and quantum sources (*13*) to integrated optical platforms. Such integrated approaches provide the advantages of compact, scalable, mass-producible, and low-cost devices (*14*). Demonstrated integrated devices include sources of heralded single photons (*15*–*17*) and entangled photon pairs (*18*), in principle allowing implementations of quantum algorithms (*19*, *20*). Here we show the parallel generation of bi- and multiphoton entangled states in a compact, integrated quantum frequency comb source.

Our quantum frequency comb is generated in a CMOS (complementary metal-oxide semiconductor)–compatible, high-refractive-index glass in a four-port microring resonator architecture [details on device fabrication and characteristics are presented in (*21*)]. The weak and anomalous dispersion of our device enables broadband phase matching for spontaneous four-wave mixing (SFWM), thereby generating a broad frequency

[1]Institut National de la Recherche Scientifique–Énergie Matériaux Télécommunications, 1650 Boulevard Lionel-Boulet, Varennes, Québec J3X 1S2, Canada. [2]Department of Physics and Astronomy, University of Sussex, Falmer, Brighton BN1 9RH, UK. [3]State Key Laboratory of Transient Optics and Photonics, Xi'an Institute of Optics and Precision Mechanics, Chinese Academy of Science, Xi'an, China. [4]Department of Physics and Materials Science, City University of Hong Kong, Tat Chee Avenue, Hong Kong, China. [5]Department of Applied Physics, Yale University, New Haven, CT 06520, USA. [6]School of Engineering and Physical Sciences, Heriot-Watt University, Edinburgh EH14 4AS, UK. [7]School of Electrical and Computer Engineering, RMIT University, Melbourne, Victoria 3001, Australia. [8]Institute of Fundamental and Frontier Sciences, University of Electronic Science and Technology of China, Chengdu 610054, China.
*These authors contributed equally to this work. **†Corresponding author. E-mail: michael.kues@emt.inrs.ca (M.K.); morandotti@emt.inrs.ca (R.M.)** ‡Present address: Racah Institute of Physics, The Hebrew University of Jerusalem, Jerusalem 91904, Israel. §Present address: Institute of Photonics, Department of Physics, University of Strathclyde, Glasgow G4 0NW, UK. ||Present address: Center for Micro-Photonics, Swinburne University of Technology, Hawthorn, Victoria 3122,Australia.

comb of photons emitted at the cavity resonances. The ring resonator's characteristics, with a high quality (Q) factor of around 240,000 (803 MHz linewidth and 200 GHz free spectral range; fig. S1), lead to high field enhancement and allow for low-power operation, while simultaneously enabling the direct generation of bright and narrow-bandwidth photons, without the need for spectral filtering of the photons (*22*, *23*). The device is pumped with a passive mode-locked fiber laser (repetition rate, 16.8 MHz), which is spectrally filtered to excite a single ring resonance at 1556.2 nm (192.65 THz) with a pulse duration of 570 ps coupled into the resonator. The pulses are directly filtered by the resonator, resulting in a perfect match between the spectral bandwidth of the pump pulses and the excited resonator mode. This in turn leads to the generation of pure single-mode photons in each resonance (*13*), confirmed by single-photon autocorrelation measurements [fig. S2 and (*21*)].

Using a high-resolution tunable C-band wavelength filter and a grating-based spectrum analyser, the single-photon spectrum was characterized at the output of the resonator (*21*). Figure 1 shows the measured single-photon count rate and the calculated photon-pair production rate per pulse as a function of wavelength. A very broad frequency comb of photons is emitted, covering the full S, C, and L bands defined by the International Telecommunication Union (wavelengths ranging from 1470 to 1620 nm). The SFWM process generates a spectrum that is symmetric in frequency, whereas the spectral asymmetry in the measured photon counts can be explained by Raman scattering, which could be further reduced by cooling the chip (*24*). As a result of the broad phase-matching condition, achieved through the close-to-zero waveguide dispersion, the emitted comb exhibits a flat and broadband spectrum with uniform pair production rates, ranging from 0.02 to 0.04 pairs per pulse, over the full measured comb.

To demonstrate an entangled quantum frequency comb, we chose time-bin entanglement, which, among several intrinsic advantages, is particularly suitable for information processing and transmission (*25*) because of its robustness (e.g., with respect to polarization fluctuations); it thus can be preserved even over long propagation distances in standard fiber networks (*26*).

Starting from the single-mode photon pairs, we generated time-bin–entangled qubits by passing the pulsed pump laser through a stabilized unbalanced fiber interferometer with a 11.4-ns delay (longer than the pulse duration of the laser), thereby producing double pulses of equal power with a defined relative phase difference. The temporal separation of the two pulses can be arbitrarily chosen, as long as it is larger than the temporal duration of the single photons; this approach thus offers considerable flexibility. The double pulses were then coupled into the integrated microring resonator (Fig. 2), where an average pump power of 0.6 mW was chosen so that the probability of creating a photon pair from both pulses simultaneously was low enough to be negligible.

This pump configuration transforms the originally single-mode photon pairs into entangled states, where the photons are in a superposition of two temporal modes. In particular, the entangled state $|\psi_{\text{time-bin}}\rangle = \frac{1}{\sqrt{2}}(|S_s, S_i\rangle + |L_s, L_i\rangle)$ is generated, where the signal (s) and idler (i) photons are in a quantum superposition of the short (*S*) and long (*L*) time bins (*21*). Most importantly, these entangled qubits are generated over all the microring resonances, thus leading to a quantum frequency comb of time-bin–entangled photon pairs.

To characterize the degree of entanglement, the generated signal and idler photons were each passed individually through a different fiber interferometer with an imbalance identical to

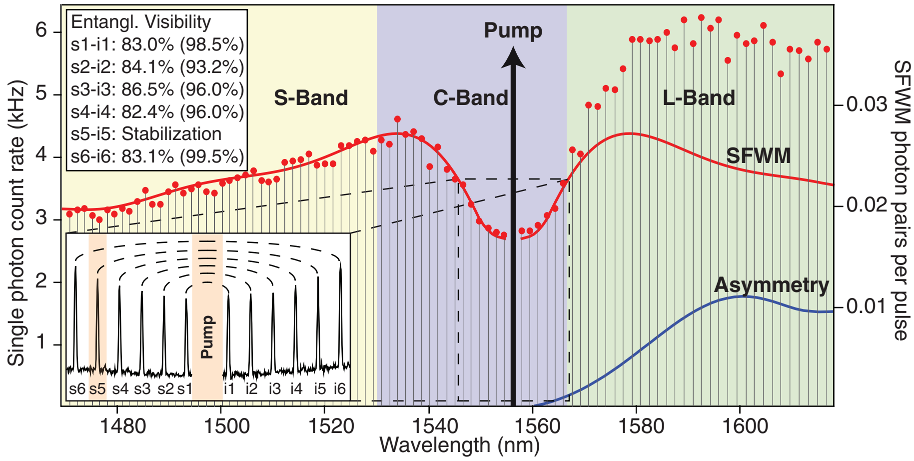

Fig. 1. Measured single-photon spectrum of the integrated quantum frequency comb. Single-photon spectrum (red circles) emitted by the microring resonator, measured using a grating-based spectrum analyzer and a high-resolution digital tunable filter in the C band (bottom inset). The S, C, and L bands are indicated. The red curve shows the symmetric contribution generated through SFWM, whereas the blue curve shows the spectral asymmetry, which can be explained by Raman scattering. The channels used in the entanglement measurements are shown in the bottom inset; the measured raw entanglement visibilities (with background-corrected values in parentheses) for the individual channel pairs are shown in the top inset.

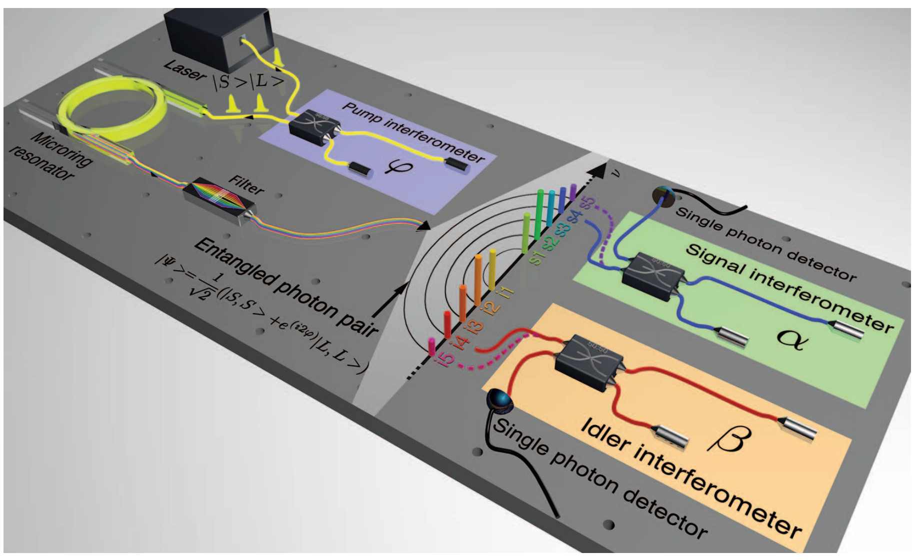

Fig. 2. Quantum frequency comb. A pulsed laser is passed through an unbalanced fiber Michelson interferometer, generating double pulses with a phase difference φ. The pulses are fed into the microring resonator, exciting one microring resonance and generating time-bin–entangled photon pairs on a frequency comb through SFWM. For the purposes of analysis [entanglement verification (Fig. 3, A to D) or quantum state tomography (Fig. 4, A and B)], each photon of the spectrally filtered photon pair is individually passed through an interferometer with the temporal imbalance equal to the time-bin separation and then detected with a single-photon detector. For the four-photon measurements (Fig. 3E and Fig. 4, C to D), four frequency modes that are symmetric to the excitation field are collected, passed through the interferometers, and spectrally filtered before detection.

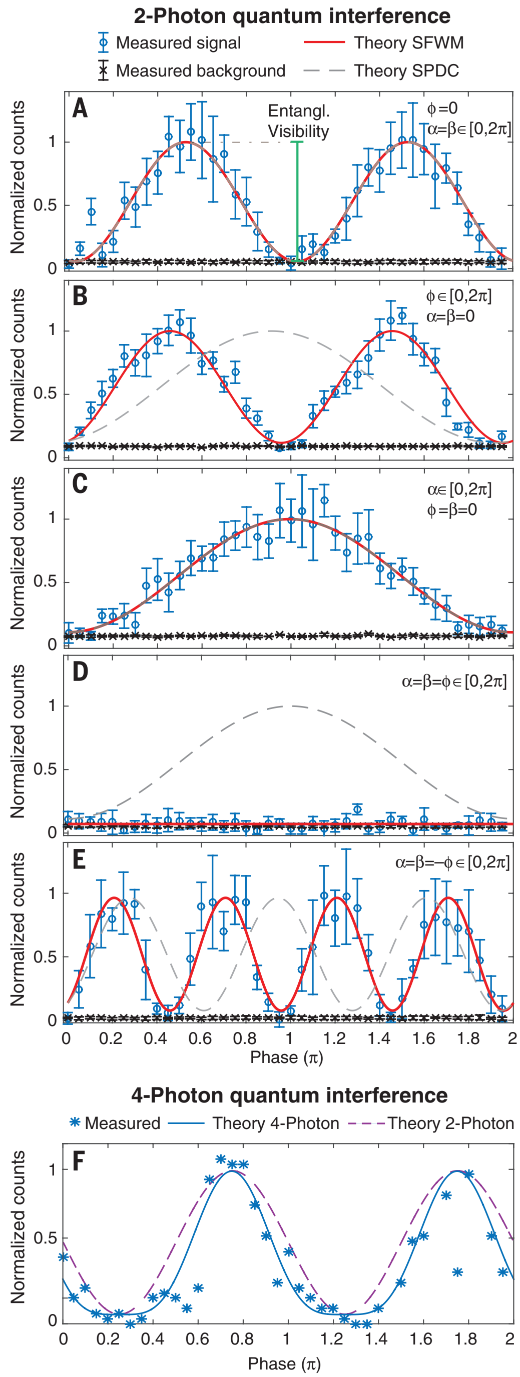

Fig. 3. Entanglement and phase control by means of SFWM. (**A** to **E**) To demonstrate the difference between the phase characteristics of SPDC and SFWM, five different quantum interference measurements were performed. Three interferometer phases were adjusted: φ, α, and β, being the phases of the pump, signal, and idler interferometers, respectively (conditions are specified in each panel). The error bars represent the standard deviation of seven measurements. (**F**) Four-photon entanglement measurement with all photon phases tuned simultaneously, showing clear four-photon quantum interference with a visibility of 89%. The solid line indicates the expected function; the dashed line shows the cosine interference in the two-photon case.

that used for the pump laser (Fig. 2). This setup allowed the measurement of the quantum interference between the signal and idler photons. For the resonances closest to the excitation frequency, we measured a photon coincidence rate of 340 Hz, which gives an estimated pair production rate of 302 kHz per channel (0.018 pairs per double pulse), accounting for system and detection losses of 14.75 dB (*21*). We selected five different frequency channel pairs within the C band (marked in Fig. 1) and recorded quantum interference with raw visibilities above 82.4%, which, being greater than $\frac{1}{\sqrt{2}} \approx 71\%$ (Fig. 1, top inset, and Fig. 3), confirm entanglement through the violation of the Clauser-Horne-Shimony-Holt (Bell-like) inequality (*27*). After subtracting the measured background (Fig. 3), the visibility was found to be above 93.2% on all channel pairs (Fig. 1, top inset).

In addition to confirming time-bin entanglement, the quantum interference also reveals the phase characteristic of the nonlinear generation process. This phase dependency has been well described in theory (*28*) and has been exploited, for example, in optical squeezing (*29*). Here we show that this phase dependency is also manifested at the single-photon level, with a clear difference between second- and third-order nonlinear interactions. When spontaneous parametric down-conversion (SPDC) in second-order nonlinear media is used to generate the entangled photon pairs, quantum interference is expected to be proportional to $1 - V\cos(\alpha + \beta + \varphi)$ (*26*), where V is the fringe visibility, φ is the pump interferometer phase, and α and β are the phases for the signal and idler interferometers, respectively. In contrast, for photons generated through SFWM (as in this work), quantum interference is expected to be of the form $1 - V\cos(\alpha + \beta - 2\varphi)$ for degenerate SFWM or $1 - V\cos(\alpha + \beta - \varphi_1 - \varphi_2)$ for nondegenerate SFWM, where φ_1 and φ_2 are the phases of the two pump fields (*21*). As shown in Fig. 3, we confirmed this important difference in phase dependency between SPDC and SFWM through five separate quantum interference measurements, where the phases of the interferometers are either tuned separately or simultaneously in a symmetric and an antisymmetric way. The expected behavior for SPDC and SFWM is plotted in Fig. 3, A to E, with dashed and solid lines, respectively. The measurements confirm the difference between the two processes, which can be explained through the additional photon involved in SFWM. In the generation of entangled photon pairs, the phase of the excitation photon (or photons) can be used to adjust the quantum state. If a single photon is involved (as in second-order processes), only the phase of this photon can be used as a control parameter. In third-order nonlinear processes, however, two photons generate the quantum state, enabling an additional control parameter (the relative phase between the two photons). Although in this study only a single excitation field was used to demonstrate the effect, exploiting two distinct nondegenerate pump fields could lead to an additional degree of freedom for the generation of all-optical reconfigurable quantum states.

The distinctive multimode characteristic of the frequency comb architecture presented here can be extended to create multiphoton entangled quantum states. By selecting two different signal-idler pairs, we can generate two-photon qubit states, given by $|\psi_1\rangle = \frac{1}{\sqrt{2}}(|S_{s1}, S_{i1}\rangle + e^{i2\varphi}|L_{s1}, L_{i1}\rangle)$ and $|\psi_2\rangle = \frac{1}{\sqrt{2}}(|S_{s2}, S_{i2}\rangle + e^{i2\varphi}|L_{s2}, L_{i2}\rangle)$. By post-selecting four-photon events with one photon on each frequency channel, these two states are multiplied, resulting in a four-photon time-bin–entangled state, given by $|\psi_{4\mathrm{photon}}\rangle = |\psi_1\rangle \otimes |\psi_2\rangle = \frac{1}{2}(|S_{s1}, S_{i1}, S_{s2}, S_{i2}\rangle + e^{i2\varphi}|S_{s1}, S_{i1}, L_{s2}, L_{i2}\rangle + e^{i2\varphi}|L_{s1}, L_{i1}, S_{s2}, S_{i2}, \rangle + e^{i4\varphi}|L_{s1}, L_{i1}, L_{s2}, L_{i2}\rangle)$. For the generation of a four-photon state, the coherence length of both photon pairs has to be the same and must be matched to the excitation field's coherence time. This requirement is intrinsically fulfilled through the resonant characteristics (equal resonance bandwidths) of the ring cavity, in combination with the excitation scheme described above. By setting the pump power to 1.5 mW, we measured a quadruple detection rate of 0.17 Hz, which corresponds to a calculated generation rate of 135 kHz, taking into account the system and detection losses of 14.75 dB. We then performed four-photon quantum interference measurements (Fig. 3F). Four-photon interference generally is not present for two completely independent

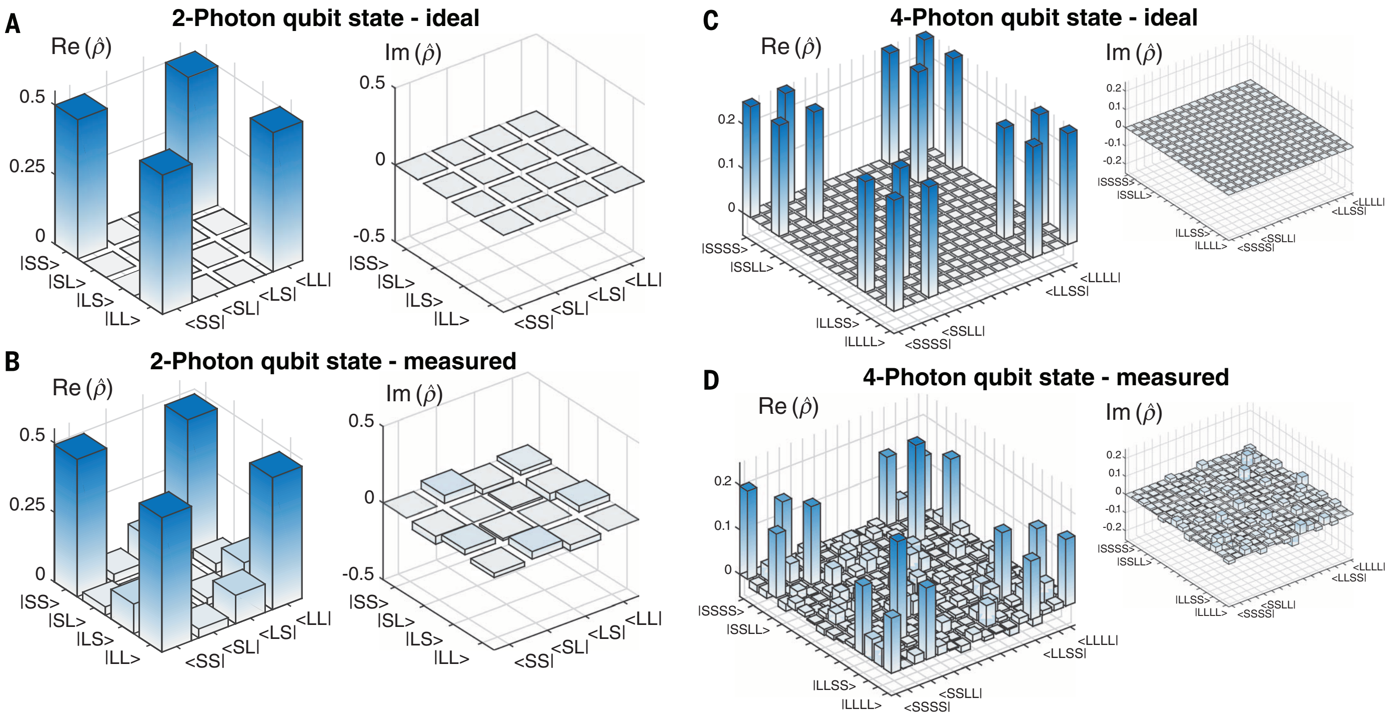

Fig. 4. Quantum state characterization by means of tomography. A quantum state can be fully described by its density matrix $\hat{\rho}$. The real (Re) and imaginary (Im) parts of the ideal density matrices of a two- and four-photon entangled qubit state are shown in (**A**) and (**C**), respectively, represented in the time-bin basis ($|SS\rangle$, $|SL\rangle$, $|LS\rangle$, $|LL\rangle$) and ($|SSSS\rangle$, $|SSSL\rangle$, ...$|LLLL\rangle$). The measured density matrix of the two-photon state (**B**) agrees very well with the ideal state, confirmed by a fidelity of 96%. The measured density matrix of the four-photon entangled qubit state (**D**) reaches a fidelity of 64%, which is comparable in quality to other nonintegrated four-photon states (*3*).

two-photon qubit states. The interference is expected to be proportional to $3 + \cos(4\alpha - 4\varphi) + 4\cos(2\alpha - 2\varphi)$, where α is the phase of all four entangled photons and φ is the pump interferometer phase (*21*). Our data follow the expected relation, having a visibility of 89% without compensation for background noise or losses. Furthermore, we repeated the four-photon measurement by selecting different combinations of four modes, always finding four-photon entanglement [fig. S3 and (*21*)].

Lastly, to fully characterize the entangled states, we performed quantum state tomography (*30*). This method measures the state density matrix, from which it is possible to extract important characteristics such as the fidelity, which describes how close the measured state is to the ideal entangled state (*21*). We first measured the two-photon qubits generated on comb lines that were symmetric with respect to the pump wavelength (Fig. 4, A and B) and found a fidelity of 96%, confirming that our generated quantum states are of high quality and very close to the ideal entangled state. For the four-photon entangled state (Fig. 4, C and D), we obtained a fidelity of 64% without compensation for background noise or interferometer imperfections, which is comparable to the fidelity measured for nonintegrated four-photon states used for practical applications (*3*).

Key characteristics of our quantum frequency comb include the intrinsic and simultaneous operation over many modes, the generation of high-purity photon pairs, the high-quality bi- and multiphoton entanglement shared among these modes, and the inherent compatibility with fiber technology. Because of these features, it has versatile and immediate applications in areas such as quantum communications and quantum computation. For example, our source can be implemented into both single-photon and entanglement-based quantum communication protocols. The broadband nature of the quantum comb is particularly attractive for multichannel applications, where the amount of transmitted data can be increased through the use of multiple, equally well-performing channels. We repeated the two-photon tomography measurement after adding 40 km of fiber and measured a fidelity of 87% [fig. S4 and (*21*)], demonstrating that the entanglement is preserved after long fiber propagation.

Furthermore, two-photon time-bin–entangled qubits have been used successfully for linear universal quantum computation (*4*, *25*), and the parallel generation and processing of multiple qubits can directly enhance such protocols where the information capacity scales with the number of comb lines used, as theoretically predicted (*25*). Even though the demonstrated multiphoton entangled states are separable, because they are generated as a product of biphoton Bell states, it is conceivable that—through the use of multiple excitation fields (*6*) or controlled phase gates (*31*)—nonseparable multiphoton cluster states could be constructed and used for measurement-based quantum computation (*3*).

Further device integration of the frequency comb will lead to more compact and stable systems with higher performances, resulting in better detection rates. All the components that were used in our setup, such as the laser, filters, interferometers, and detectors (connected via optical fibers), could be integrated on a single chip (*13*) to reduce size and losses (currently at 14.75 dB). An easily realized decrease in losses by 5 dB would increase the four-photon detection rate by a factor of 100, and an achievable loss reduction of 10 dB would increase it to the useful kilohertz range.

Our results indicate that integrated quantum frequency comb sources based on third-order nonlinearities can open up new venues for the generation and control of complex quantum states, thus providing a scalable and practical platform for optical quantum information processing.

REFERENCES AND NOTES

1. H. J. Kimble, *Nature* **453**, 1023–1030 (2008).
2. D. Deutsch, *Proc. R. Soc. A Math. Phys. Eng. Sci.* **400**, 97 (1985).
3. P. Walther *et al.*, *Nature* **434**, 169–176 (2005).
4. P. C. Humphreys *et al.*, *Phys. Rev. Lett.* **111**, 150501 (2013).
5. M. Kolobov, *Rev. Mod. Phys.* **71**, 1539–1589 (1999).
6. M. Chen, N. C. Menicucci, O. Pfister, *Phys. Rev. Lett.* **112**, 120505 (2014).
7. M. Pysher, Y. Miwa, R. Shahrokhshahi, R. Bloomer, O. Pfister, *Phys. Rev. Lett.* **107**, 030505 (2011).
8. J. Roslund, R. M. de Araújo, S. Jiang, C. Fabre, N. Treps, *Nat. Photonics* **8**, 109–112 (2013).
9. N. C. Menicucci, *Phys. Rev. Lett.* **112**, 120504 (2014).
10. M. D. Eisaman, J. Fan, A. Migdall, S. V. Polyakov, *Rev. Sci. Instrum.* **82**, 071101 (2011).
11. W. Wieczorek *et al.*, *IEEE J. Sel. Top. Quantum Electron.* **15**, 1704–1712 (2009).

12. T. J. Kippenberg, R. Holzwarth, S. A. Diddams, *Science* **332**, 555–559 (2011).
13. D. Bonneau, J. W. Silverstone, M. G. Thompson, in *Silicon Photonics III*, L. Pavesi, D. J. Lockwood, Eds. (Springer, ed. 3, 2016), pp. 41–82.
14. D. J. Moss, R. Morandotti, A. L. Gaeta, M. Lipson, *Nat. Photonics* **7**, 597–607 (2013).
15. S. Azzini *et al*., *Opt. Express* **20**, 23100–23107 (2012).
16. C. Reimer *et al*., *Nat. Commun.* **6**, 8236 (2015).
17. N. C. Harris *et al*., *Phys. Rev. X* **4**, 041047 (2014).
18. D. Grassani *et al*., *Optica* **2**, 88 (2015).
19. A. Politi, M. J. Cryan, J. G. Rarity, S. Yu, J. L. O'Brien, *Science* **320**, 646–649 (2008).
20. J. C. F. Matthews, A. Politi, A. Stefanov, J. L. O'Brien, *Nat. Photonics* **3**, 346–350 (2009).
21. Materials and methods are available as supplementary materials on *Science* Online.
22. Z. Ou, Y. Lu, *Phys. Rev. Lett.* **83**, 2556–2559 (1999).
23. C. Reimer *et al*., *Opt. Express* **22**, 6535–6546 (2014).
24. A. S. Clark *et al*., *Opt. Express* **20**, 16807 (2012).
25. T. Pittman, *Physics* **6**, 110 (2013).
26. J. Brendel, N. Gisen, W. Tittel, H. Zbinden, *Phys. Rev. Lett.* **82**, 2594–2597 (1999).
27. J. F. Clauser, M. A. Horne, A. Shimony, R. A. Holt, *Phys. Rev. Lett.* **23**, 880–884 (1969).
28. C. C. Gerry, P. L. Knight, *Introductory Quantum Optics* (Cambridge Univ. Press, 2005).
29. Z. Y. Ou, S. F. Pereira, H. J. Kimble, K. C. Peng, *Phys. Rev. Lett.* **68**, 3663–3666 (1992).
30. D. F. V. James, P. G. Kwiat, W. J. Munro, A. G. White, *Phys. Rev. A* **64**, 052312 (2001).
31. G. Vallone, E. Pomarico, P. Mataloni, F. De Martini, V. Berardi, *Phys. Rev. Lett.* **98**, 180502 (2007).

ACKNOWLEDGMENTS

This work was supported by the Natural Sciences and Engineering Research Council of Canada (NSERC) through the Steacie Memorial Fellowship and Discovery Grants programs and by the Australian Research Council Discovery Projects program. C.R. and P.R. acknowledge the support of a NSERC Vanier Canada Graduate Scholarship and a NSERC Alexander Graham Bell Canada Graduate Scholarship (Master's), respectively. M.K. acknowledges support from FRQNT (Fonds de Recherche du Québec–Nature et Technologies) through the MELS fellowship program (Merit Scholarship Program for Foreign Students; Ministère de l'Éducation, de l'Enseignement Supérieur et de la Recherche du Québec). M.K. also acknowledges funding from the European Union's Horizon 2020 research and innovation program under Marie Sklodowska-Curie grant agreement no. 656607. We acknowledge support from the People Programme (Marie Curie Actions) of the European Union's 7th Framework Programme for Research and Technological Development [B.W. under Research Executive Agency (REA) grant agreement no. 625466 and L.C. under REA grant agreement no. 627478]. F.G. acknowledges support from Mitacs through the Accelerate Program. S.T.C. acknowledges support from the CityU SRG-Fd (Strategic Research Grant for fundable Competitive Earmarked Research Grant) program #7004189. We thank R. Helsten for the mechanical design of the interferometer housing; P. Saggu for assisting in the measurement of the single-photon spectrum; L. La Volpe for assisting in the evaluation of the tomography measurement; J. Azaña, T. A. Denidni, S. O. Tatu, and L. Razzari for providing some of the required experimental equipment; and A. Tavares, A. Yurtsever, and M. A. Gauthier for helpful discussions. Special thanks go to QuantumOpus and N. Bertone of OptoElectronics Components for their help and for providing us with state-of-the-art photon detection equipment.

SUPPLEMENTARY MATERIALS

www.sciencemag.org/content/351/6278/1176/suppl/DC1
Materials and Methods
Supplementary Text
Figs. S1 to S4
References (*32*–*37*)

12 November 2015; accepted 5 February 2016
10.1126/science.aad8532

SPIN MODELS

Simple universal models capture all classical spin physics

Gemma De las Cuevas[1]* and Toby S. Cubitt[2]

Spin models are used in many studies of complex systems because they exhibit rich macroscopic behavior despite their microscopic simplicity. Here, we prove that all the physics of every classical spin model is reproduced in the low-energy sector of certain "universal models," with at most polynomial overhead. This holds for classical models with discrete or continuous degrees of freedom. We prove necessary and sufficient conditions for a spin model to be universal and show that one of the simplest and most widely studied spin models, the two-dimensional Ising model with fields, is universal. Our results may facilitate physical simulations of Hamiltonians with complex interactions.

The description of systems with many interacting degrees of freedom is a ubiquitous problem across the natural and social sciences. Be it electrons in a material, neurons interacting through synapses, or speculative agents in a market, the challenge is to simplify the system so that it becomes tractable while capturing some of the relevant features of the real system. Spin models are one way of addressing this challenge. Originally introduced in condensed matter physics in order to study magnetic materials (*1*–*4*), they have permeated many other disciplines, including quantum gravity (*5*), error-correcting codes (*6*), percolation theory (*3*), graph theory (*7*), neural networks (*8*), protein folding (*9*), and trading models in stock markets (*10*).

Spin models are microscopically simple, yet their versatile interactions lead to a very wide variety of macroscopic behavior. Formally, a spin model is specified by a set of degrees of freedom, the "spins," and a cost function, or "Hamiltonian," H that specifies the interaction pattern as well as the type and strength of interactions among the spins. (In physics, the Hamiltonian specifies the energy of each possible spin configuration; in other contexts, this energy value may quantify a more abstract "cost" associated with a configuration.)

This definition encompasses a wide range of models, including attractive and/or repulsive interactions, regular and irregular interaction patterns, models in different spatial dimensions, models with different symmetries (for example, "conventional" spin models with global symmetries versus models with local symmetries, such as lattice gauge theories), many-body interactions [such as vertex models and edge models (*11*)], and more. We will use the word "model" to refer to a (generally infinite) family of spin Hamiltonians. Different Hamiltonians within the same model are typically related in some natural way. For example, the "two-dimensional (2D) Ising model with fields" is the family of Hamiltonians of the form

$$H_G(\sigma) = \sum\nolimits_{\langle i,j\rangle} J_{ij}\sigma_i\sigma_j + \sum\nolimits_i r_i\sigma_i \qquad (1)$$

where $\sigma = \sigma_1, \sigma_2, \ldots, \sigma_n$ is a configuration of Ising (two-level) spins $\sigma_i \in \{-1, 1\}$ on a 2D square lattice, $\langle i,j\rangle$ denotes neigbouring spins, and J_{ij} and r_i are real numbers specifying the coupling strengths and local fields, respectively.

Here, we show that there exist certain spin models, which we call universal, whose low-energy sector can reproduce the complete physics of any other classical spin model. What does it mean to "reproduce the complete physics"? Informally, we say that a spin model with Hamiltonian H simulates a target Hamiltonian H' if (i) the energy levels of H below a threshold Δ reproduce the energy levels of H'; (ii) there is a fixed subset P of the spins of H—which we call the "physical spins"—whose configuration for each energy level below Δ reproduces the spin configuration of the corresponding energy level of H'; and (iii) the partition function of H reproduces that of H'. From the partition function, one can derive all equilibrium thermodynamical properties of the system. A universal model is then a model that can simulate any other spin model.

We denote spin degrees of freedom—discrete or continuous—by a string of spin states $\sigma = \sigma_1, \sigma_2, \ldots, \sigma_n$. For q-level Ising spins (discrete degrees of freedom with a finite number q of distinct states), we can label the states arbitrarily by integers: $\sigma_i \in \{1, \ldots, q\}$. For continuous spins, a spin state is represented by a

[1]Max Planck Institute for Quantum Optics, Hans-Kopfermann-Strasse 1, 85748 Garching, Germany. [2]Department of Computer Science, University College London, Gower Street, London WC1E 6EA, UK.
*Corresponding author. E-mail: gemma.delascuevas@mpq.mpg.de

Generation of multiphoton entangled quantum states by means of integrated frequency combs
Christian Reimer, Michael Kues, Piotr Roztocki, Benjamin Wetzel, Fabio Grazioso, Brent E. Little, Sai T. Chu, Tudor Johnston, Yaron Bromberg, Lucia Caspani, David J. Moss and Roberto Morandotti
(March 10, 2016)
Science **351** (6278), 1176-1180. [doi: 10.1126/science.aad8532]

Editor's Summary

Entangled frequency combs

The ability to generate optical frequency combs in which the output light is made up of millions of sharp lines precisely spaced apart has been important for optical applications and for fundamental science. Reimer *et al.* now show that frequency combs can be taken into the quantum regime. They took individual teeth of the combs and quantum-mechanically entangled them to form complex optical states. Because the method is compatible with existing fiber and semiconductor technology, the results demonstrate a possible scalable and practical platform for quantum technologies.

Science, this issue p. 1176